Supplementary Information for

Structural basis of human VANGL-PRICKLE interaction

Yanyi Song, Shuyi Jian, Junlin Teng, Pengli Zheng*, and Zhe Zhang*

*Correspondence should be addressed to zhengpl@pku.edu.cn or zzhang01@pku.edu.cn.

The PDF file includes:

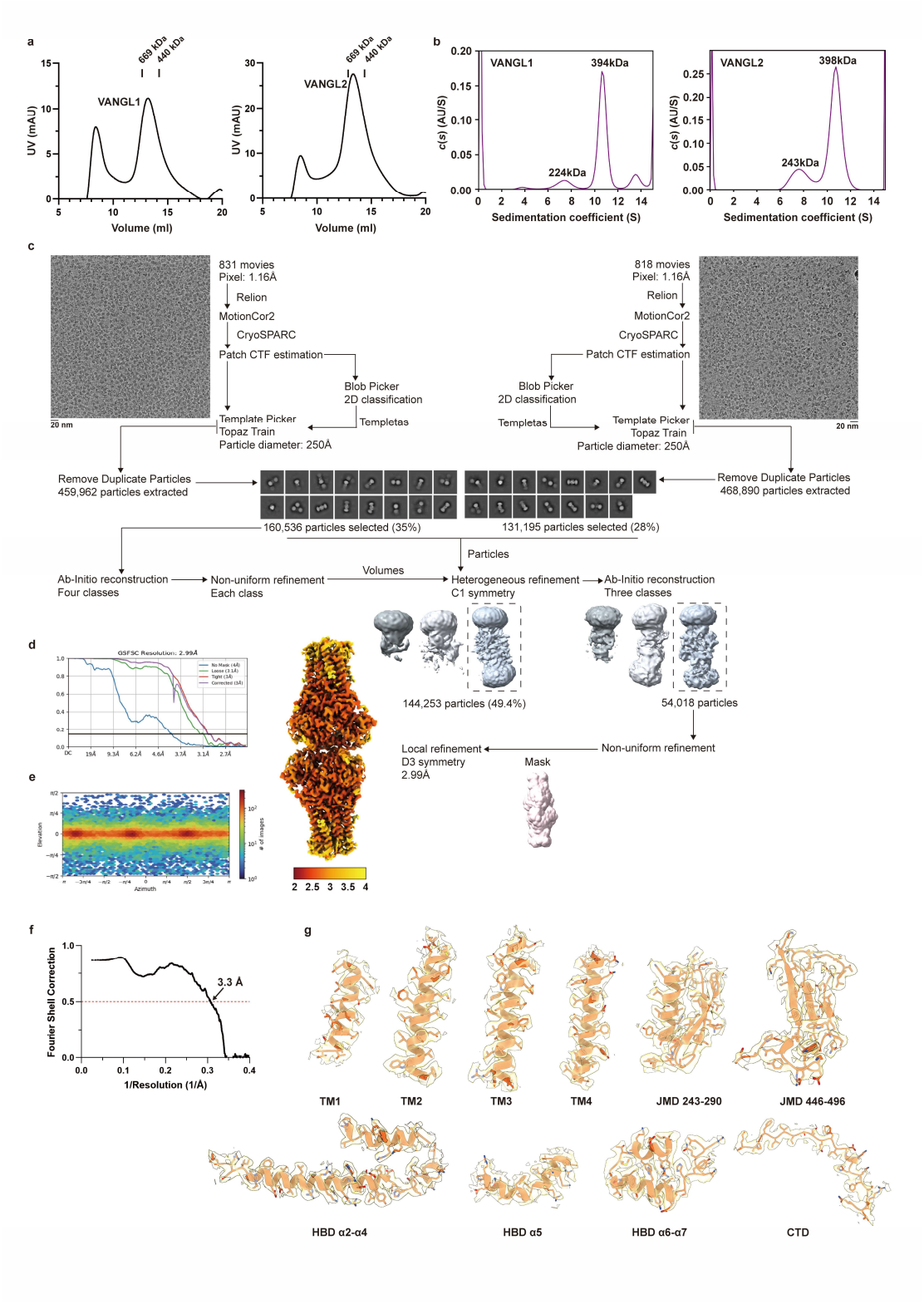

Supplementary Fig. 1 Characterization of the VANGL oligomerization status and the cryo-EM data processing of the VANGL1 dataset.

a, Size exclusion chromatography (SEC) profiles of VANGL1 (left) and VANGL2 (right). **b,**

Analytical ultracentrifugation (AUC) analyses of VANGL1 (left) and VANGL2 (right). **c-g,** Cryo-EM data processing of the VANGL1 dataset. **c,** Workflow of the data processing and local resolution of the cryo-EM map. The contour level of the sharpened map is 0.48. **d,** Fourier shell correlation (FSC) curves between two half maps. **e,** Orientation distribution of the particles used in the final reconstruction. **f,** FSC curve calculated between the cryo-EM map and structural model. **g,** Close-up view of the cryo-EM densities and fitted atomic models for representative regions of the structure.

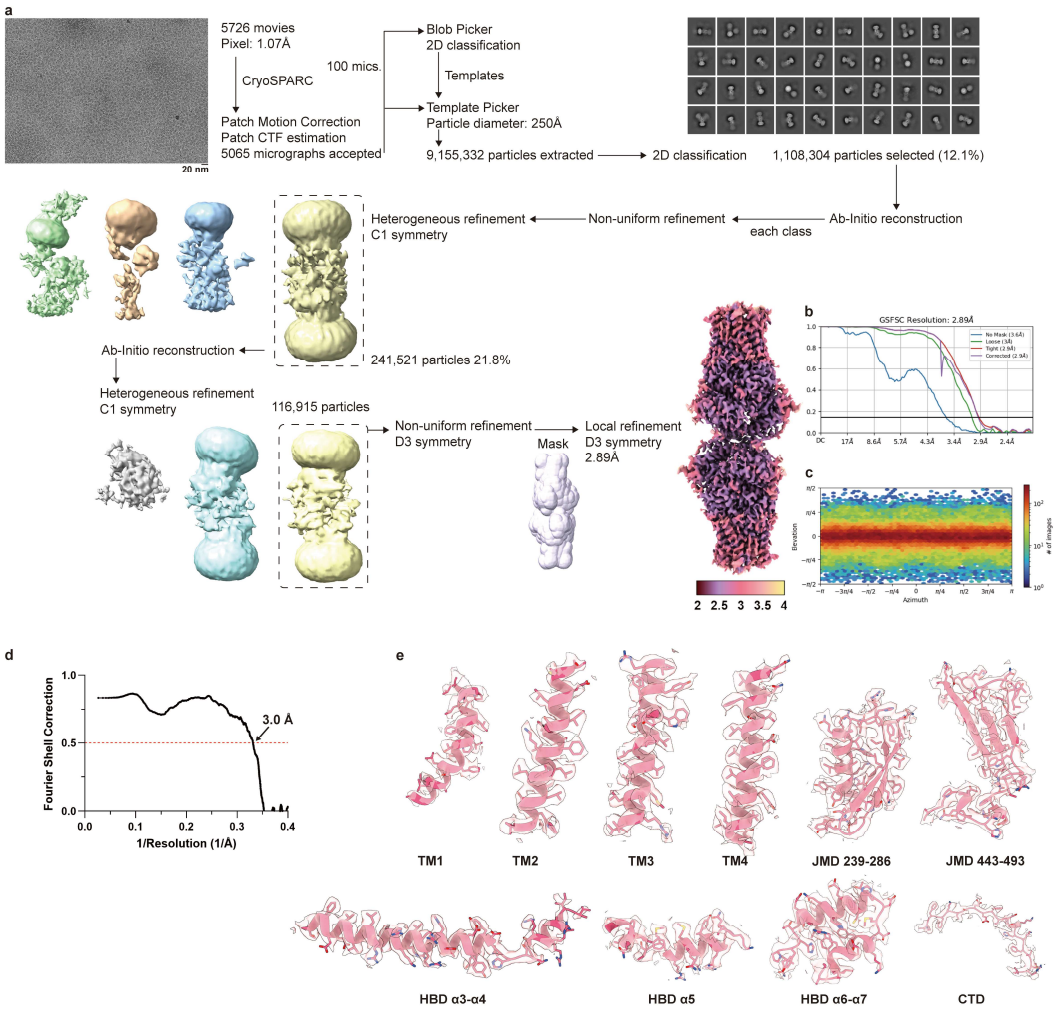

Supplementary Fig. 2 Cryo-EM data processing of the VANGL2 dataset.

a, Workflow of the data processing and the local resolution of the cryo-EM map. The contour level of the sharpened map is 0.187. **b,** Fourier shell correlation (FSC) curves between two half maps. **c,** Orientation distribution of the particles used in final reconstruction. **d,** FSC curve calculated between the cryo-EM map and structural model. **e,** Close-up view of the cryo-EM densities and fitted atomic models for representative regions of the structure.

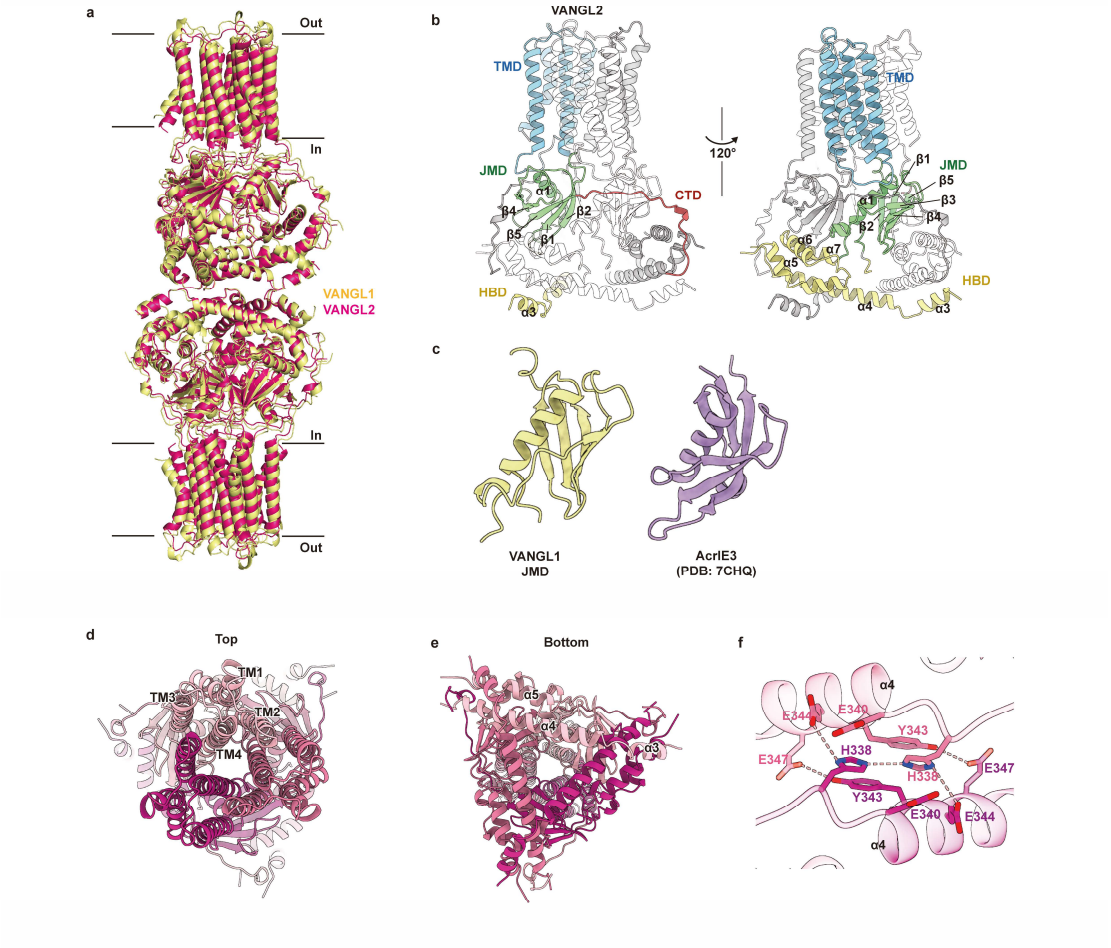

Supplementary Fig. 3 Structural details of the VANGL hexamer.

a, Superposition of the VANGL1 and VANGL2 structures. **b,** Assembly of the VANGL2 trimer. One VANGL2 subunit is colored by different domains. The other two subunits are colored in white and grey, respectively. The TMD, JMD, HBD, and CTD are represented in blue, green, yellow, and red, respectively. **c,** Structures of the assembled JMD in VANGL1 and the AcrIE3 protein (PDB: 7CHQ). **d** and **e,** Top (**d**) and bottom (**e**) views of the VANGL2 trimer. **f,** Interaction details between two VANGL2 trimers for their hexamer assembly. Residues involved in their interaction are shown with side chains. Dashed lines represent hydrogen bond interactions (< 4.0 Å).

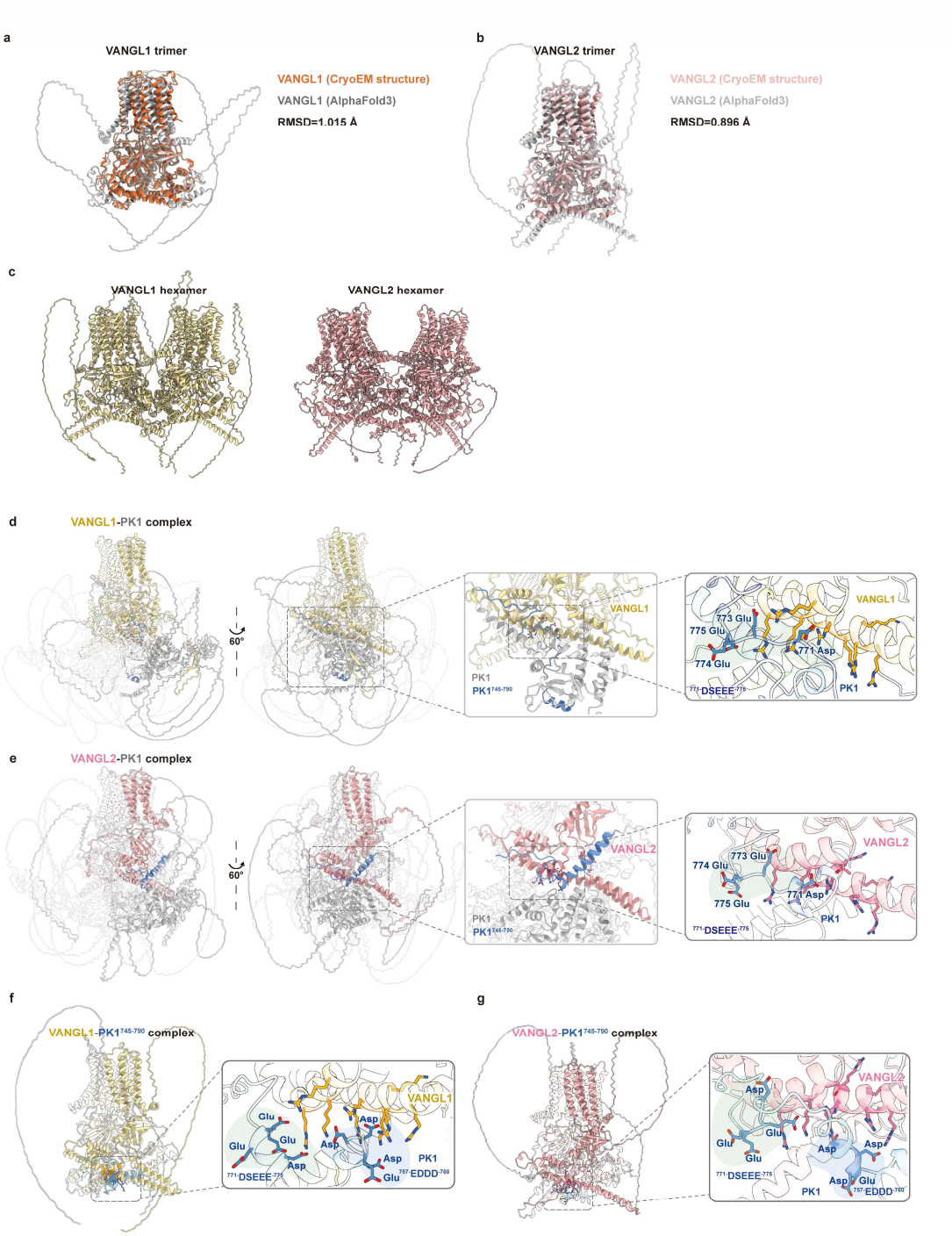

Supplementary Fig. 4 AlphaFold3 predictions for the VANGL oligomers and the complexes of VANGL with PK1 and PK1$^{745-790}$.

a and **b,** The structural comparison between the VANGL trimers predicted by AlphaFold3 (gray) and the structures determined in our study (VANGL1, orange; VANGL2, pink). **c,** The AlphaFold3 prediction for VANGL hexamers. **d** and **e,** The AlphaFold3 prediction for the VANGL-PK1

complexes. VANGL1 is colored in yellow, VANGL2 is in pink, PK1 is in gray, and the VANGL interaction region of PK1 ($PK1^{745-790}$) is in blue. The proposed interaction sites based on the experiment results are shown with side chains. **f** and **g,** The AlphaFold3 prediction for the VANGL-$PK1^{745-790}$ complexes are presented with VANGL1 colored in yellow, VANGL2 is in pink, and $PK1^{745-790}$ is in blue. The proposed interaction sites are shown with side chains.

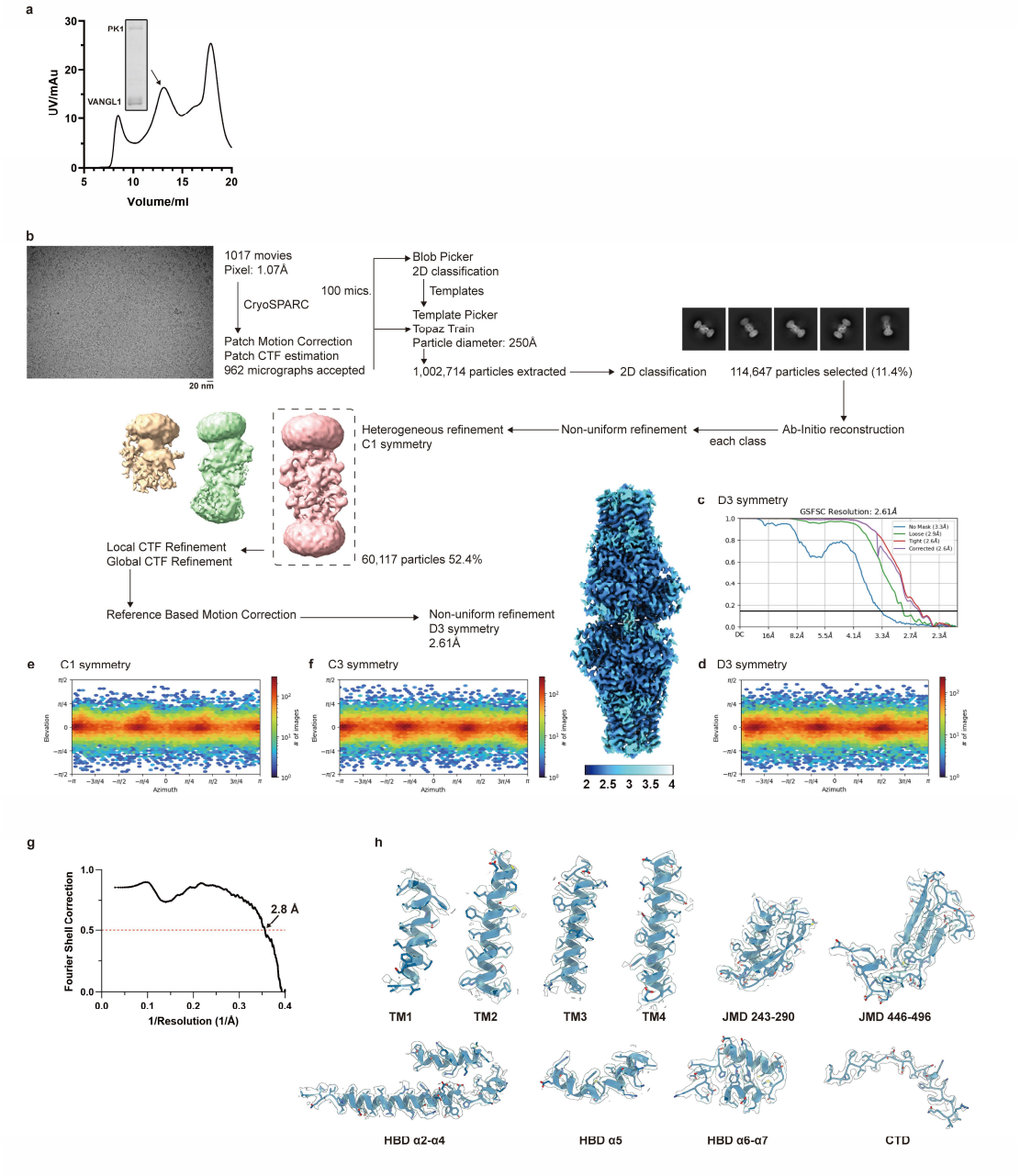

Supplementary Fig. 5 Cryo-EM data processing of the VANGL1-PK1 dataset.

a, Profile of the size exclusion chromatography (SEC) and SDS-PAGE results of the VANGL1-PK1 complex. **b,** Workflow of the data processing and the local resolution of the cryo-EM map. The contour level of the sharpened map is 0.1. **c,** Fourier shell correlation (FSC) curves between two half maps. **d-f,** Orientation distribution of the particles used in final reconstruction corresponding to D3 (**d**), C1 (**e**), and C3 symmetry (**f**). **g,** FSC curve calculated between the cryo-EM map and

structural model. **h,** Close-up view of the cryo-EM densities and fitted atomic models for representative regions of the structure. Source data are provided as a Source Data file.

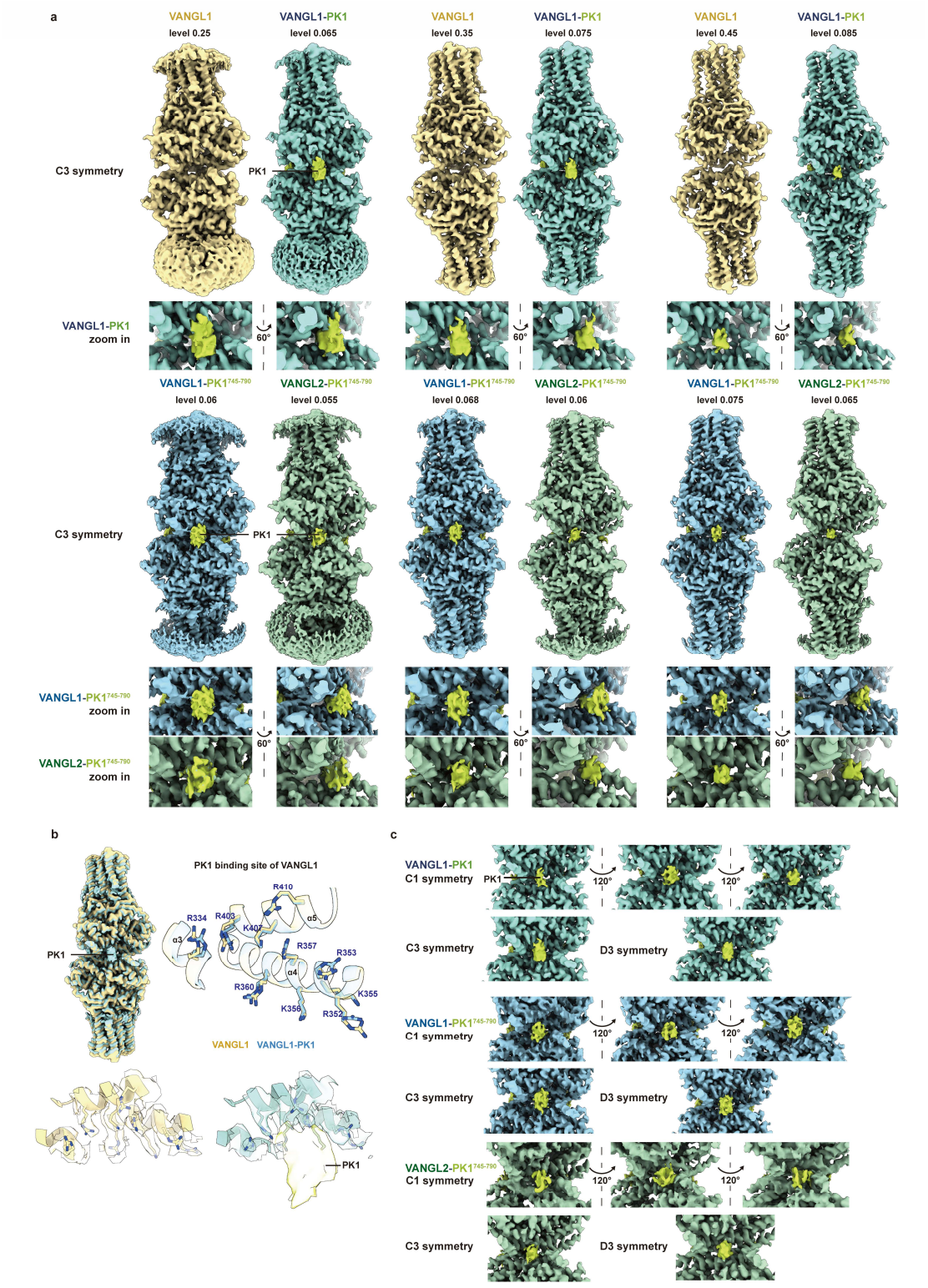

Supplementary Fig. 6 Density features of PK1 and PK1 peptides in the cryo-EM maps refined with different symmetries and displayed at various contour levels.

a, A side-by-side comparison of the PK1 density features at different contour level. The maps were

refined with C3 symmetry. **b,** The structural comparison of the side chain conformations at the PK1 binding site of VANGL1. It is noted that no significant conformational changes were observed upon PK1 binding. The VANGL1 structure is colored in yellow, while the VANGL1-PK1 structure is in blue. The residues on the proposed PK1-binding interface of VANGL1 are shown with side chains. **c,** The density features of PK1 are compared across the C1, C3, and D3 symmetry maps.

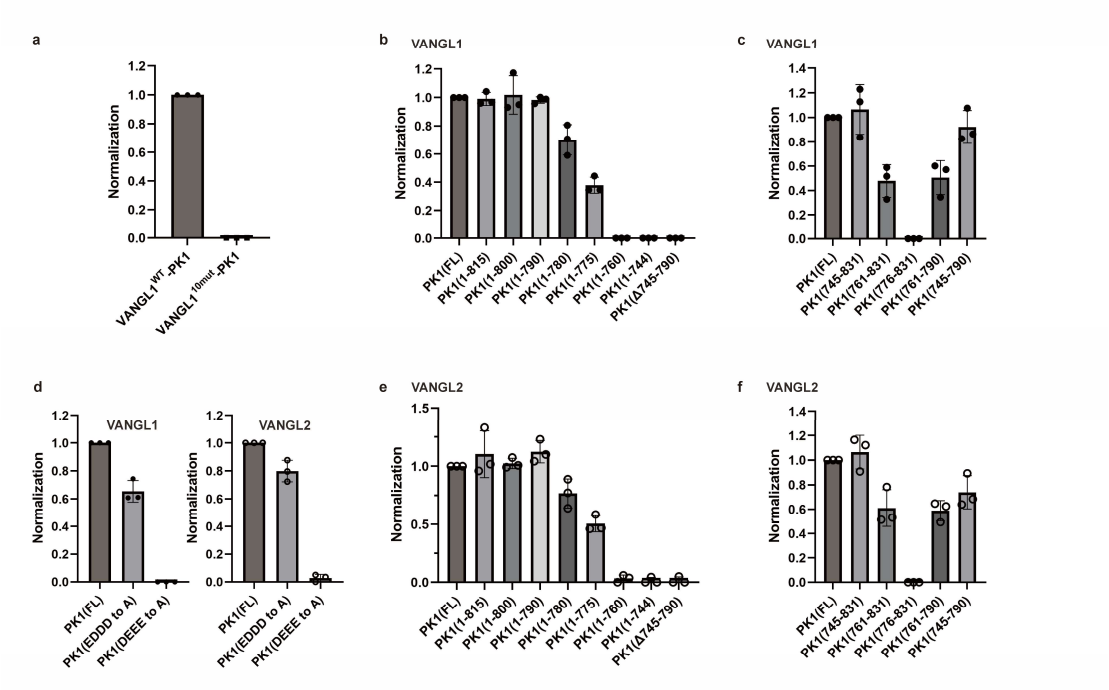

Supplementary Fig. 7 Quantifications of the pull-down results in Fig. 3b-g.

All experiments were performed in triplicate. The quantifications were processed using ImageJ. The fluorescence images were first separated into red and green channels. Subsequently, the threshold value was fine-tuned to ensure the optimal image analysis. Then the GFP to mCherry intensity ratio was calculated for each experimental group, taking into account of the input values. Finally, all measurements were normalized relative to the VANGL(WT)-PK1(FL) control. Source data are provided as a Source Data file.

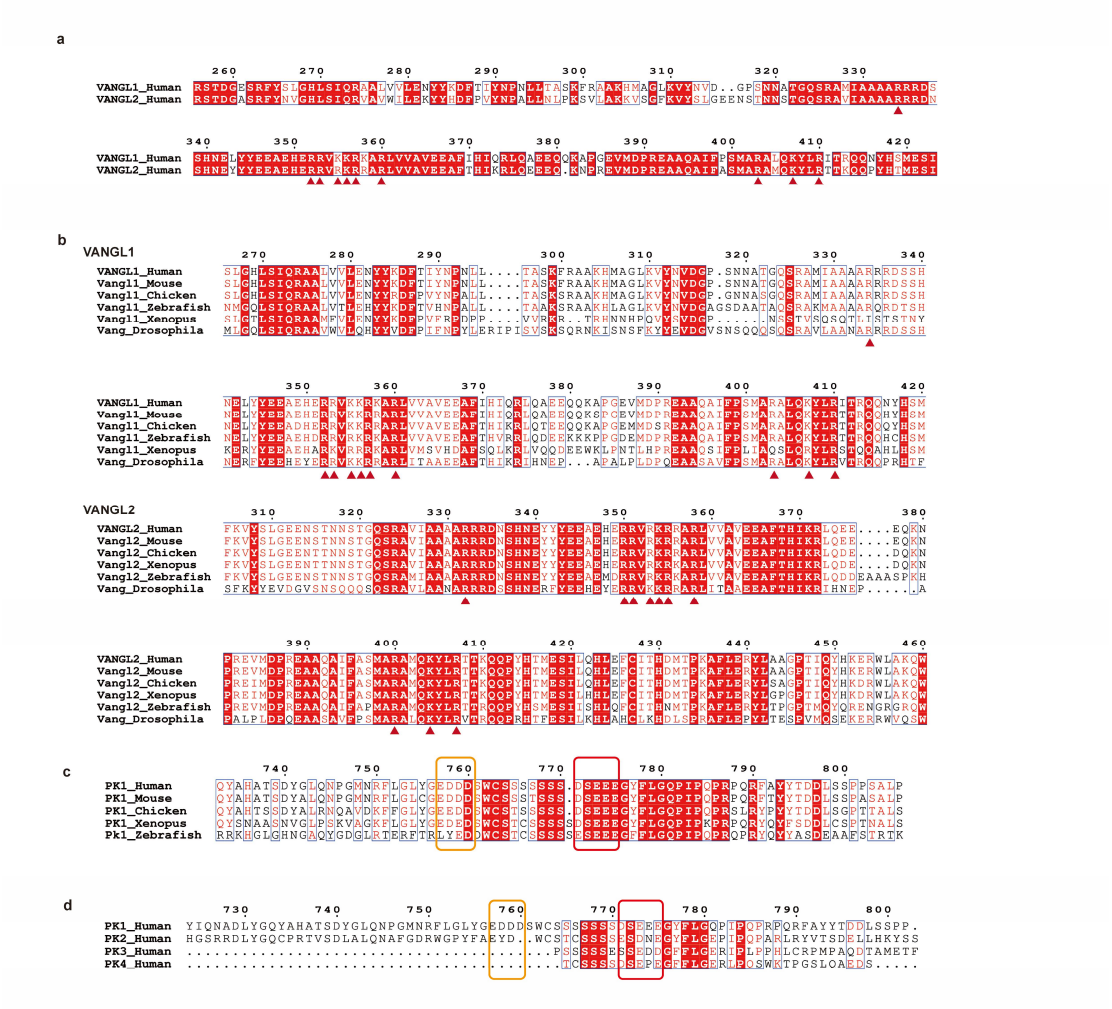

Supplementary Fig. 8 Sequence alignment of the VANGL and PK analogs.

a, Sequence alignment of human VANGL1 and VANGL2. The residues involved in PK1 interaction are indicated with red arrows. **b,** Sequence alignment of Vangl1 or Vangl2 among several representative species. The residues involved in PK1 interaction are indicated with red arrows. **c,** Sequence alignment of Pk1 among several representative species. The auxiliary and major regions for VANGL binding are indicated with orange and red boxes, respectively. **d,** Sequence alignment of human PK1-4. The auxiliary and major regions for VANGL binding are indicated.

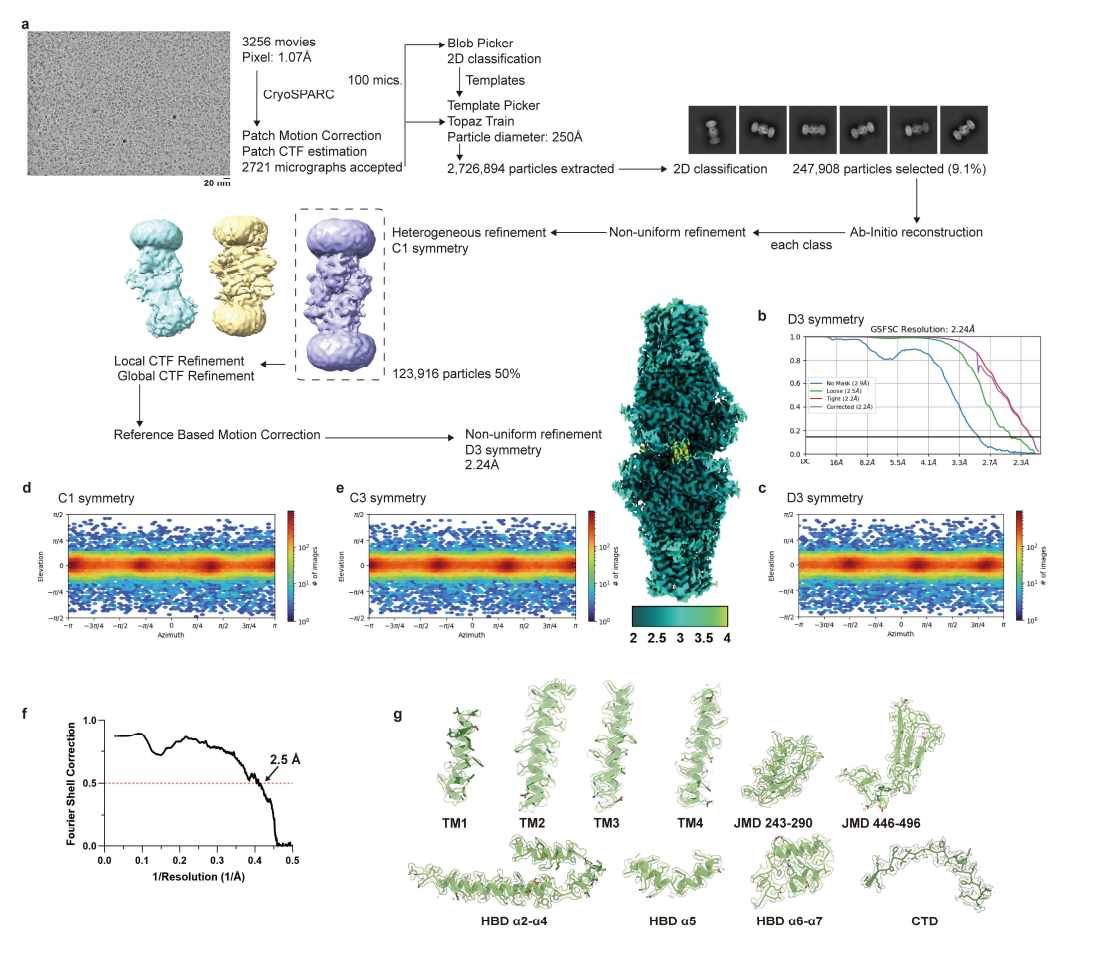

Supplementary Fig. 9 Cryo-EM data processing of the VANGL1-PK1$^{745\text{-}790}$ dataset.

a, Workflow of the data processing and the local resolution of the cryo-EM map. The contour level of the sharpened map is 0.09. **b,** Fourier shell correlation (FSC) curves between two half maps. **c-e,** Orientation distribution of the particles used in final reconstruction corresponding to D3 (**c**), C1 (**d**), and C3 symmetry (**e**). **f,** FSC curve calculated between the cryo-EM map and structural model. **g,** Close-up view of the cryo-EM densities and fitted atomic models for representative regions of the structure.

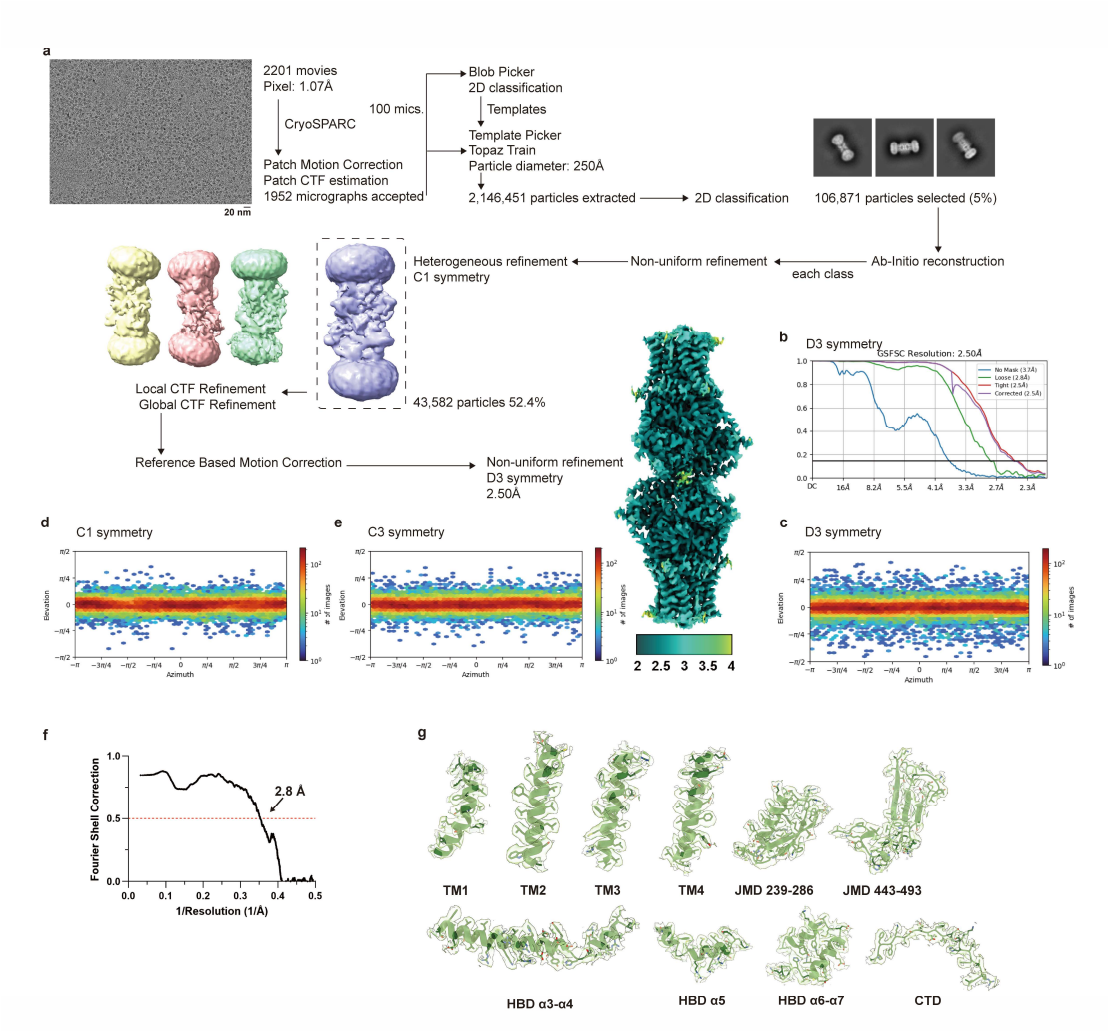

Supplementary Fig. 10 Cryo-EM data processing of the VANGL2-PK1$^{745\text{-}790}$ dataset.

a, Workflow of the data processing and the local resolution of the cryo-EM map. The contour level of the sharpened map is 0.074. **b,** Fourier shell correlation (FSC) curves between two half maps. **c-e,** Orientation distribution of the particles used in final reconstruction corresponding to D3 (**c**), C1 (**d**), and C3 symmetry (**e**). **f,** FSC curve calculated between the cryo-EM map and structural model. **g,** Close-up view of the cryo-EM densities and fitted atomic models for representative regions of the structure.

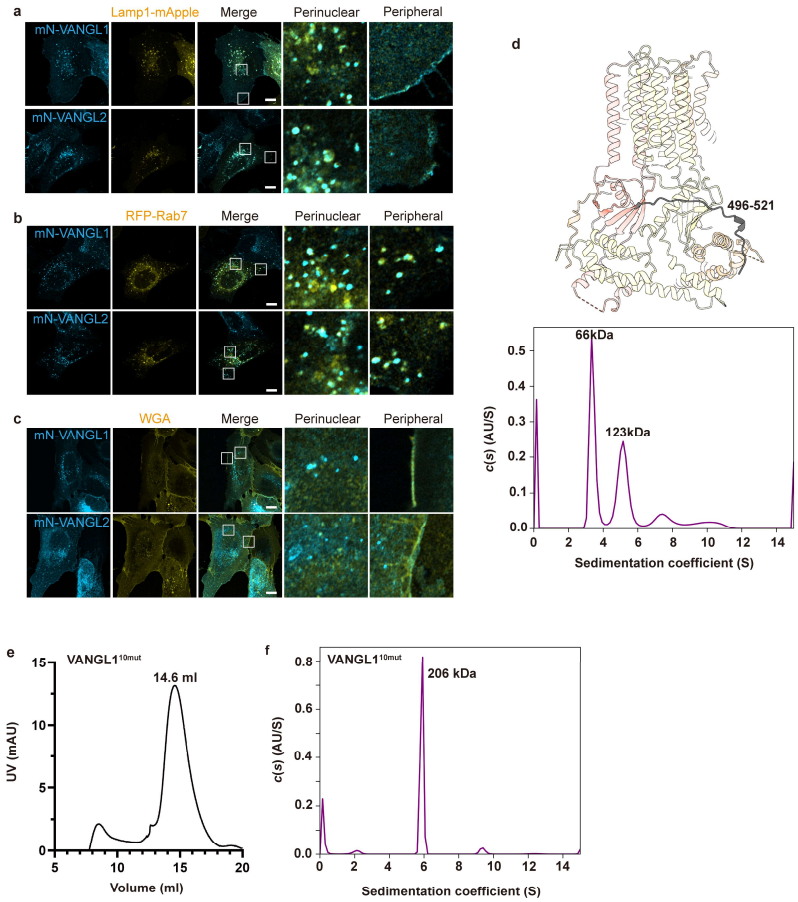

Supplementary Fig. 11 Localization of exogenous VANGLs and characterization of the oligomerization states of VANGL1$^{1\text{-}495}$ and VANGL1^{10mut}.

a, Representative images of U2OS cells co-expressing mN-VANGL1/2 (Cyan) and Lamp1-mApple (Yellow). **b,** Representative images of U2OS cells co-expressing mN-VANGL1/2 (Cyan) and RFP-Rab7 (Yellow). **c,** Representative images of U2OS cells expressing mN-VANGL1/2 in which WGA (Yellow) was also stained. For **a-c**, perinuclear and peripheral regions (outlined) are enlarged on the right. Scale bars in (**a-c**): 10 μm. **d,** Schematic summary of VANGL1$^{1\text{-}495}$ and its quantitative analysis using AUC. **e,** Gel filtration profile of VANGL1^{10mut}. **f,** AUC analysis of VANGL1^{10mut}.

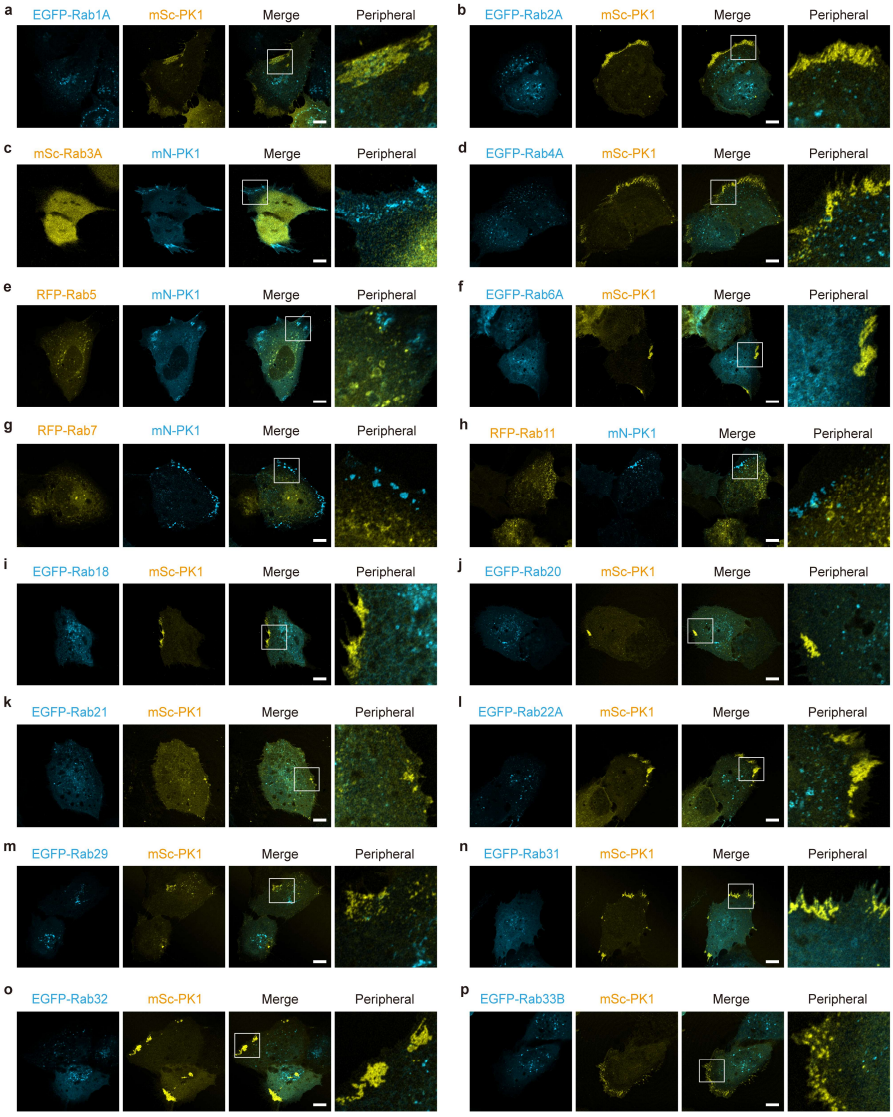

Supplementary Fig. 12 Cell imaging of the PK1 and various Rab proteins.

Representative images of U2OS cells co-expressing mN-PK1/mSc-PK1 and various Rab proteins, including EGFP-Rab1A, EGFP-Rab2A, mSc-Rab3A, EGFP-Rab4A, RFP-Rab5, EGFP-Rab6A, RFP-Rab7, RFP-Rab11, EGFP-Rab18, EGFP-Rab20, EGFP-Rab21, EGFP-Rab22A, EGFP-Rab29, EGFP-Rab31, EGFP-Rab32, and EGFP-Rab33B. Peripheral regions (outlined) are enlarged on the right. Scale bars: 10 μm.

Supplementary Table 1 Cryo-EM data collection, refinement, and validation statistics of the VANGL1, VANGL2, and VANGL1-PK1 samples.

	VANGL1 (EMD-61545) (PDB 9JK6)	VANGL2 (EMD-61546) (PDB 9JK7)	VANGL1-PK1 (EMD-61547) (PDB 9JK8)
Data collection and processing			
Magnification	36,000	81,000	81,000
Voltage (kV)	200	300	300
Electron exposure (e^{-}/Å^2)	60	60	60
Defocus range (μm)	1.0-1.8	1.0-1.8	1.0-1.8
Pixel size (Å)	1.16	1.07	1.07
Symmetry imposed	D3	D3	D3
Initial particle images (no.)	928,852	9,155,332	1,002,714
Final particle images (no.)	54,018	116,915	60,117
Map resolution (Å)	3.0	2.9	2.6
FSC threshold	0.143	0.143	0.143
Map resolution range (Å)	2.6-5.8	2.4-5.3	2.4-4.7
Refinement			
Initial model used (PDB code)	-	-	-
Model resolution (Å)	3.3	3.0	2.8
FSC threshold	0.5	0.5	0.5
Model resolution range (Å)	-	-	-
Map sharpening *B* factor (Å^2)	-84.3	-76.6	-81.4
Model composition			
Non-hydrogen atoms	18,504	17,820	18,504
Protein residues	2,256	2,172	2,256
Ligands	-	-	-
B factors (Å^2)			
Protein	69.60	40.03	65.34
Ligand	-	-	-
R.m.s. deviations			
Bond lengths (Å)	0.005	0.005	0.005
Bond angles (°)	0.867	0.669	0.822
Validation			
MolProbity score	1.14	1.60	1.83
Clashscore	3.49	12.11	13.62
Poor rotamers (%)	0.00	0.00	0.00
Ramachandran plot			
Favored (%)	98.65	99.16	96.89
Allowed (%)	1.35	0.84	3.11
Disallowed (%)	0.00	0.00	0.00

Supplementary Table 2 Cryo-EM data collection, refinement, and validation statistics of the VANGL1-PK1$^{745-790}$ and VANGL2-PK1$^{745-790}$ samples.

	VANGL1-PK1$^{745-790}$ (EMD-61548) (PDB 9JK9)	VANGL2-PK1$^{745-790}$ (EMD-61549) (PDB 9JKA)
Data collection and processing		
Magnification	81,000	81,000
Voltage (kV)	300	300
Electron exposure (e^{-}/Å^2)	60	60
Defocus range (μm)	1.0-1.8	1.0-1.8
Pixel size (Å)	1.07	1.07
Symmetry imposed	D3	D3
Initial particle images (no.)	2,726,894	2,146,451
Final particle images (no.)	123,916	43,582
Map resolution (Å)	2.2	2.5
FSC threshold	0.143	0.143
Map resolution range (Å)	2.2-3.8	2.4-5.4
Refinement		
Initial model used (PDB code)	-	-
Model resolution (Å)	2.5	2.8
FSC threshold	0.5	0.5
Model resolution range (Å)	-	-
Map sharpening *B* factor (Å^2)	-66.8	-63.0
Model composition		
Non-hydrogen atoms	18,582	17,820
Protein residues	2,268	2,172
Ligands	-	-
B factors (Å^2)		
Protein	54.68	73.47
Ligand	-	-
R.m.s. deviations		
Bond lengths (Å)	0.007	0.007
Bond angles (°)	1.238	1.206
Validation		
MolProbity score	1.49	1.22
Clashscore	5.96	4.45
Poor rotamers (%)	0.00	0.00
Ramachandran plot		
Favored (%)	97.04	98.60
Allowed (%)	2.96	1.40
Disallowed (%)	0.00	0.00

Supplementary Table 3 Loss-of-function or disease-related mutations identified in VANGL proteins.

VANGL1		VANGL2	
R274Q	Kibar et al. (2007)[1]	D255E	Kibar et al. (2001)[2]
M328T		S464N	
V239I		S84F	Lei et al. (2010)[3]
S83L	Kibar et al. (2009)[4]	R353C	
F153S		F437S	
R181Q		R105H	Kibar et al. (2011)[5]
L202F		R135W	
A404S		R177H	
R173H	Bartsch et al. (2012)[6]	V178I	
R186H		L242V	
G205R		T247M	
A187V	Merello et al. (2015)[7]	R270H	
D389H		R482H	
R517H			
F440V	Andersen et al. (2017)[8]		
I136N			

Supplementary References

1 Kibar, Z. *et al.* Mutations in *VANGL1* Associated with Neural-Tube Defects. *New England Journal of Medicine* **356**, 1432-1437, doi:10.1056/NEJMoa060651 (2007).

2 Kibar, Z. *et al.* Ltap, a mammalian homolog of Drosophila Strabismus/Van Gogh, is altered in the mouse neural tube mutant Loop-tail. *Nature Genetics* **28**, 251-255, doi:10.1038/90081 (2001).

3 Lei, Y.-P. *et al.* VANGL2 Mutations in Human Cranial Neural-Tube Defects. *New England Journal of Medicine* **362**, 2232-2235, doi:10.1056/NEJMc0910820 (2010).

4 Kibar, Z. *et al.* Novel mutations inVANGL1in neural tube defects. *Human Mutation* **30**, E706-E715, doi:10.1002/humu.21026 (2009).

5 Kibar, Z. *et al.* Contribution of VANGL2 mutations to isolated neural tube defects. *Clinical Genetics* **80**, 76-82, doi:10.1111/j.1399-0004.2010.01515.x (2011).

6 Bartsch, O. *et al.* Novel VANGL1 Gene Mutations in 144 Slovakian, Romanian and German Patients with Neural Tube Defects. *Molecular Syndromology* **3**, 76-81, doi:10.1159/000339668 (2012).

7 Merello, E. *et al.* Expanding the mutational spectrum associated to neural tube defects: literature revision and description of novel VANGL1 mutations. *Birth Defects Res A Clin Mol Teratol* **103**, 51-61, doi:10.1002/bdra.23305 (2015).

8 Andersen, M. R. *et al.* Mutation of the Planar Cell Polarity Gene VANGL1 in Adolescent Idiopathic Scoliosis. *Spine* **42**, E702-E707, doi:10.1097/brs.0000000000001927 (2017).